Science and Technology Indonesia
e-ISSN:2580-4391 *p*-ISSN:2580-4405
Vol. 9, No. 3, July 2024

Research Paper

Nichrome Dependency in Welding Layer Using *In situ* Fabrication on Hardness and Corrosion Properties

Syaripuddin[1*], Sopiyan[1], Muhammad Fauzan Perdana Putra[1], Maman Kartaman Ajiriyanto[2], Sigit Dwi Yudanto[3], Muhammad Yunan Hasbi[3], Ferry Budhi Susetyo[1]

[1] *Department of Mechanical Engineering, Universitas Negeri Jakarta, Jakarta, 13220, Indonesia*
[2] *Research Center for Nuclear Material and Radioactive Waste Technology - National Research and Innovation Agency, KST B.J. Habibie, South Tangerang, 15314, Indonesia*
[3] *Research Center for Metallurgy - National Research and Innovation Agency, KST B.J. Habibie, South Tangerang, 15314, Indonesia*
***Corresponding author**: syaripuddin_andre@unj.ac.id

Abstract

The use of shielded metal arc welding (SMAW) equipment to synthesize alloys is one of the most promising methods as it can be used for in-situ fabrication. The hardness and corrosion properties of the deposited layer during the welding process can be enhanced by dilution of nichrome (NiCr) during the process. Therefore, the alloy was synthesized on the surface of the mild steel using SMAW equipment with various NiCr additions. The properties of the alloy were investigated using an X-ray diffraction (XRD), an Optical microscope, a Potentiostat, and a Vickers hardness apparatus. The appearance of martensite overlaps with the ferrite phase could be affected by the addition of NiCr to the alloy. An increase in NiCr content is followed by an increase in the lattice parameter value of the ferrite phase. The presence of a certain amount of nickel (Ni) contributes to the formation of lower transformation phases, including martensite. At the same time, the incorporation of chromium (Cr) also plays a significant role in promoting the formation of acicular ferrite. An increase in NiCr content in NiCr2 and NiCr3 samples results in a quantitative increase in martensite formation. Adding 0.434 g of NiCr to the weld deposited layer could result in the corrosion rate of the alloy being 0.1118 mm/y. Higher hardness is found in the NiCr3 sample, around 742.06 HV.

Keywords

Alloys, Dilution, Welding Process, Martensite, Corrosion Rate

Received: 7 March 2024, Accepted: 23 May 2024
`https://doi.org/10.26554/sti.2024.9.3.651-659`

1. INTRODUCTION

The construction of infrastructure in the coastal area requires heavy equipment such as excavators for material transportation. To operate an excavator in a coastal area, it is important to have a component that has good corrosion resistance and hardness properties (Kuptsov et al., 2021). Improving their hardness and corrosion resistance is necessary to extend the life of excavator blades (Das et al., 2021; Okechukwu et al., 2018).

Various methods were used to solve the problems, such as coating, alloy synthesis, and heat treatment processes (Liu et al., 2020; Wang et al., 2015). Recently, alloy synthesis has been conducted using welding equipment. Compared to other alloy syntheses methods, this process is both innovative and cost-effective. In addition, welding equipment is a promising method for alloy synthesis as it can be applied in situ. There have been several studies on alloy synthesis in situ with welding equipment (de Almeida et al., 2016; Justus Panicker and Senthilkumar, 2023; Ma et al., 2015). The process of shielded metal arc welding (SMAW) can be easily done. SMAW equipment is frequently used in heavy equipment workshops because of its small size and easy movement. Furthermore, in situ alloy synthesis has been successfully achieved by previous research using the SMAW equipment (Singh et al., 2020; Sopiyan et al., 2024; Syaripuddin et al., 2023).

Nichrome (NiCr) alloy has good mechanical and corrosion properties (Kumar et al., 2020; Li et al., 2021). By diluting NiCr onto the weld layer during the welding process, it could enhance its hardness and corrosion properties. Justus Panicker and Senthilkumar (2023) added NiCr in the welding layer using a rotational arc-based dual wire arc, which could enhance the tensile strength and corrosion resistance properties of the sample. Wang et al. (2023a) conducted alloy fabrication between rare earth Y and NiCr filler alloy using the vacuum brazing process over copper (Cu) pot and found the chromium (Cr) element diffuses in the molten metal and combines with the carbon (C) element to form carbide. Moreover, with increased Cr content, various carbides such as Cr_3C_2, and Cr_7C_3 were formed (Wang et al., 2023a). According to Xu et al. (2022), these carbides could enhance the strength properties of the material. Galchenko et al. (2019) successfully added NiCr powder when joining Cu and steel plates using electron-beam welding, resulting in a weld joint hardness of 350 to 700 HV. Huang et al. (2015), made a composite coating of mixed powder NiCrBSi, NiCr−Cr_3C_2, and WC using plasma spray welding resulting in carbide content in the coating increased with increasing the NiCr NiCr−Cr_3C_2 and WC mass fraction in the mixed powders. Saeedi et al. (2021) conducted laser cladding of NiCr and NiCr−TiC composited over AISI 420, and resulting NiCr and NiCr−TiC deposited has lower weight loss than AISI 420.

HV 600 is a commercial electrode that can be applied single, double, and triple layers over steel using SMAW equipment which resulted in the hardness between 440-540, 520-600, and 540-675 HV, respectively (Nikko Steel, 2014). Besides the amount of layers, the current and polarity that were set in the SMAW equipment during synthesis also influenced the hardness of the formed deposited layer. Many efforts have been conducted to enhance the deposited layer properties when welding using an HV 600 electrode such as heat treatment, and the additional amount of titanium (Ti) or NiCr in the deposited layer during welding. A previous study conducted direct quenching in various media (engine oil and palm oil) of the deposited layer where welded by HV 600 over mild steel, resulting in higher hardness of the deposited layer when quenched in palm oil (Syaripuddin et al., 2023). Moreover, previous research also welded over carbon steel using an HV 600 electrode and adding three pieces of Ti wire (150 × ∅ 0.65 mm) into the deposited layer during welding resulting in enhanced hardness from 503.48 to 686.1 HV (Syaripuddin et al., 2023). Furthermore, previous research welded carbon steel using an HV 600 electrode and adding NiCr wire around 2.52 g into the deposited layer during welding resulting in a corrosion rate and hardness is 0.337 mm/y and 581 HV (Sopiyan et al., 2024).

Dilution of NiCr onto the deposited layer during the welding process has been proven to enhance its hardness and corrosion properties. Unfortunately according to previous research corrosion resistance and hardness of the deposited layer do not reach optimal conditions (Sopiyan et al., 2024). Therefore, the present research focuses on the varying composition of NiCr that is added to the deposited layer during welding using the SMAW process with an HV 600 electrode. This research aims to deeply explore the hardness and corrosion behavior of the formed alloy in the deposited layer. The X-ray diffraction (XRD), Optical microscope, Potentiostat, and Vickers hardness apparatus were used to determine the structure, microstructure, electrochemical behavior, and hardness value of the deposited layer.

2. EXPERIMENTAL SECTION

2.1 Materials

In the present work, were used carbon steel, NiCr, and HV 600 as the base material (75×10×10 mm), NiCr addition, and filler metal, respectively, which were similar to the previous study (Sopiyan et al., 2024; Syaripuddin et al., 2023). The NiCr wire was cut and weighed for approximately 0.434, 0.844, and 1.292 grams to be added to the deposited layer.

2.2 Methods

The HV 600 filler metal was dried in an oven at 150°C for 1 hour prior to welding (Nikko Steel, 2014). Each weighed NiCr wire (0.434, 0.844, and 1.292 g) was placed on the top surface of the base material and the samples were namely NiCr1, NiCr2, and NiCr3. Afterward, the single-layer welding process was performed using SMAW (Fro BF 443), DCEP, and 90 A. The natural cooling process for samples was carried out after the welding was completed.

2.3 Characterizations

The formed alloys were checked using XRD, Optical microscope, Potentiostat, and Vickers hardness apparatus. XRD was performed from 20-110° using PANalytical Aeris (CoK$\alpha\lambda$ = 1.7890 Åand step size 0.0217°). The Rietveld method was utilized to determine the lattice parameters, which included phase composition, using XRD data. Furthermore, to investigate the microstructure of the alloy, it was mounted in epoxy resin, polished, and etched with 2% Nital. It was later obtained using an Optical microscope (Olympus BX53M).

A Potentiostat (Gamry References 600) was used to investigate the electrochemical behavior of the alloy in 3.5% NaCl solution at 25°C which is near to simulated seawater (Pauzi et al., 2023). The electrochemical behavior of the sample was investigated through open circuit potential (OCP), potentiodynamic polarization, and electro-impedance spectroscopy (EIS) measurements. Firstly, OCP measurements were performed until 1200s to evaluate the stability voltage of various samples. Then, the potentiodynamic polarization was scanned at a rate of 1 mV/s. Where the sample is the working electrode, Platinum (Pt) is the counter electrode, and saturated calomel is the reference electrode. Following the potentiodynamic polarization measurement, Tafel extrapolation was used to determine the corrosion current density (I_{corr}) and potential (E_{corr}). The corrosion rate (*Corr Rate*) was found from the Equation (1) (Syamsuir et al., 2023).

$$Corr\,Rate(mm/y) = \frac{C(M \times i_{corr})}{n\rho} \tag{1}$$

Where *Corr Rate* is corrosion rate (mm/y), C is corrosion rate constant (mm/y), M is atomic weight (g/mol), I_{corr} is corrosion current density (A/cm^2), n is the number of electrons involved, and ρ is density (g/cm^3). Furthermore, the electro-impedance spectroscopy (EIS) was performed at 0.05 sd 4500 HZ to obtain the Nyquist and Bode plot.

Finally, various samples were tested using an FV-300e Vickers hardness tester with a load of 5 kg. A total of ten repeatable tests were carried out. The average hardness value is presented in Figure 8.

3. RESULTS AND DISCUSSION

3.1 Phase and Structure Analysis

Figure 1 shows the diffraction pattern of carbon steel samples after the addition of NiCr filler during the welding process. Based on the diffraction reflection of the three samples, it appears that the substance belongs to the ferrite phase ($\alpha-$Fe) with a body center cubic (bcc) crystal system. Ferrite and Fe oxide (Fe_3O_4) phases were present in the NiCr1 sample. The results are similar to the ferrite phase peaks reported by Elena Astafurova and Soliz (Astafurova et al., 2023; Soliz et al., 2022) at angles of 2θ = 52.03, 77.12, and 99.37°. The appearance of a martensite phase (α'$-$Fe) at an angle of 2θ, which overlaps with the ferrite phase, can be influenced by the addition of NiCr filler during the welding process. This area exhibits an asymmetric pattern with overlapping peaks, as seen in Figure 1. An asymmetric pattern and peak broadening indicate that there are two distinct phases: ferrite and martensite phases (Tanaka et al., 2020; Zhang et al., 2017). The asymmetric pattern increases at a peak angle of 2θ=52° in the NiCr3 sample. Additionally, it can be observed in the NiCr3 diffraction pattern that the ferrite phase peak has been shifted and its intensity has decreased. A higher content of the martensite phase could be qualitatively. According to the evidence, the NiCr3 sample has the greatest change in shift and intensity drop. The shift indicates that NiCr filler may have replaced the ferrite phase, which could result in lattice distortion. The NiCr3 sample also had other phases like the FeO_2 phase detected.

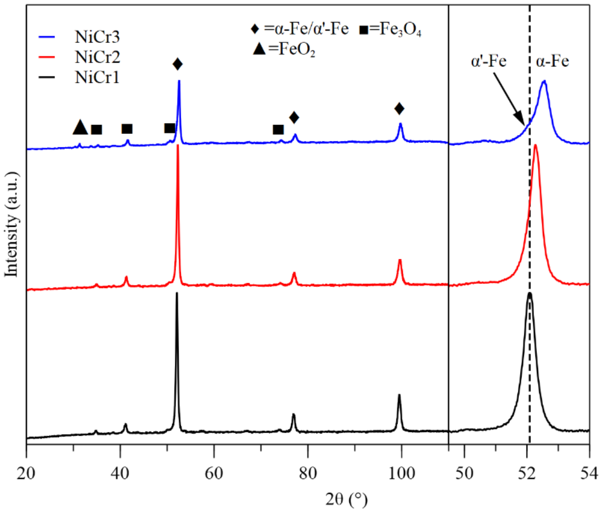

Figure 1. XRD Curve of Various Samples

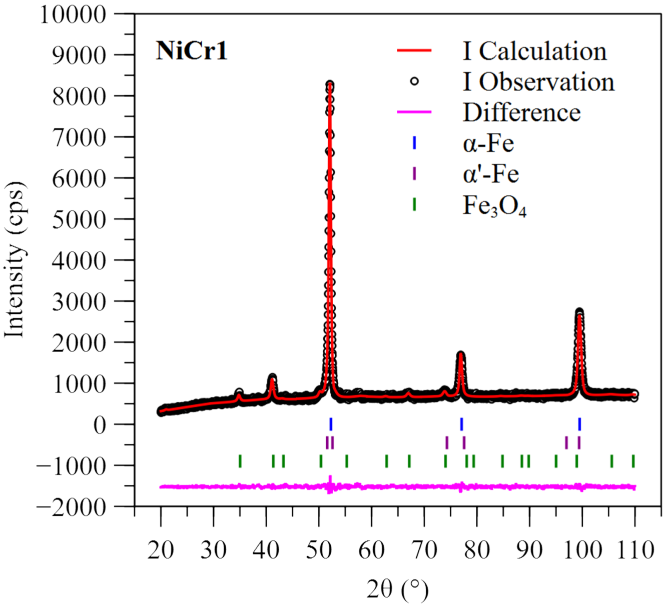

Figure 2. Plot of the Observation vs Calculation Diffraction Pattern of the NiCr1 Sample

Through refinement of the X-ray diffraction pattern, the Rietveld method was used to analyze the crystal structure of the samples. The diffraction pattern and calculations for the NiCr1 sample are compared in Figure 2. Quantitative calculation is done by calculating the phases of ferrite, martensite, and Fe_3O_4. According to the calculation results, the martensite phase fraction of all three samples has increased. The martensite content in this study is also higher than what was reported in earlier studies (BNU sample) (Syaripuddin et al., 2023). Table 1 displays the composition of each phase of the three samples. The calculation results indicate that the NiCr1 sample has a ferrite phase with a lattice parameter value of 2.8709 Å. The lattice parameter values of the ferrite phase are identical to those published by Soliz et al. (2022). Increase in NiCr content followed by an increase in the lattice parameter value of the ferrite phase. For the NiCr2 and NiCr3 samples, the lattice parameters of the ferrite phase are 2.8713 Åand 2.8724 Å, respectively. The crystallographic data for the three samples can be found in Table 1.

3.2 Microstructure of Weld Layer

Figure 3 represents the microstructure of various deposited layers. The light optical micrographs in Figures 3 (b) and (c) reveal the presence of martensite in the NiCr2 and NiCr3 samples. Generally, the formation of the martensite phase occurs spontaneously due to rapid cooling. This rapid cooling hinders the decomposition of austenite into ferrite and cementite through diffusion (Li et al., 2022). In the welding process, the rapid cooling phenomenon may occur due to the temperature difference between the weld metal and the electrode or filler. Moreover, the presence of a certain amount of nickel (Ni) contributes to the formation of lower transformation phases, including martensite (Kong et al., 2019; Umale et al., 2019). The martensite phase appears as a dark brown constituent lo-

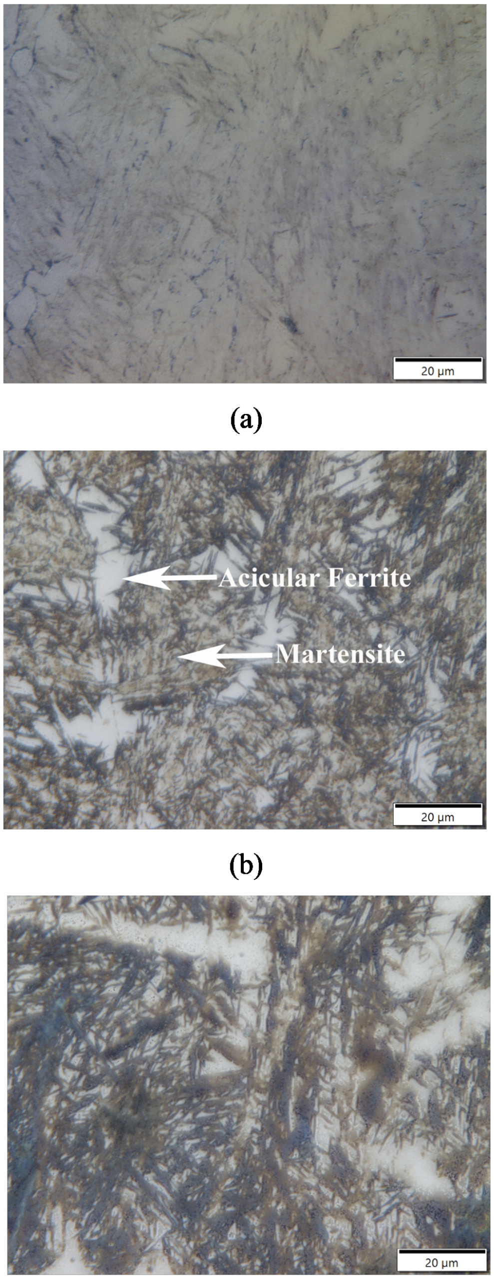

(a)

(b)

(c)

Figure 3. Microstructure of Weld Layer (a) NiCr1, (b) NiCr2, and (c) NiCr3

cated on top of the white-colored acicular ferrite phase. The welding process employed resulted in the formation of acicular ferrite as the primary phase of the weld metal (Durmuşoğlu et al., 2015; Jorge et al., 2018). Additionally, the incorporation of Cr also plays a significant role in promoting the formation of acicular ferrite (Lee and Lee, 2015). On the other hand, the NiCr1 sample exhibits no martensite formation. This is likely attributed to the insufficient critical cooling rate to reach the martensite start temperature (Ms), leading to the retention of the parent phase (ferrite). This observation is further supported by the XRD results discussed earlier. Furthermore, the increased NiCr content leads to a qualitative enhancement in martensite formation within the NiCr2 and NiCr3 samples. This is further corroborated by the observed increase in the intensity of the α'−Fe martensite phase in the XRD results. This enhancement is also attributed to the influence of Ni, which plays a role in reducing the critical cooling rate and consequently leads to an improvement in the mechanical properties

Table 1. Crystallographic Data of Various Samples

Source	NiCr1	NiCr2	NiCr3
Ferrite ($\alpha-$Fe) phase	System crystal: cubic Space group: im-3m		
Phase fraction (wt.%)	66.69	58.16	49.67
Lattice -a=b=c (Å)	2.8709	2.8713	2.8724
Martensite (α'$-$Fe) phase	System crystal: tetragonal Space group: i4/mmm		
Phase fraction (wt.%)	23.65	31.28	34.91
Lattice -a=b (Å	2.8561	2.8606	2.8595
Lattice -c (Å)	2.9623	2.9558	2.9363
Fe_3O_4 phase	System crystal: cubic Space group: fd-3m		
Phase fraction (wt.%)	9.66	10.56	8.74
Lattice -a=b=c (Å)	8.4041	8.3847	8.4014
FeO_2 phase	System crystal: orthorhombic Space group: A m a m		
Phase fraction (wt.%)	n/a	n/a	6.68
Lattice -a (Å)	n/a	n/a	3.8942
Lattice -b (Å)	n/a	n/a	12.6481
Lattice -c (Å)	n/a	n/a	3.0405
λ^2	1.219	1.303	1.378
wRp (%)	4.09	4.19	5.48

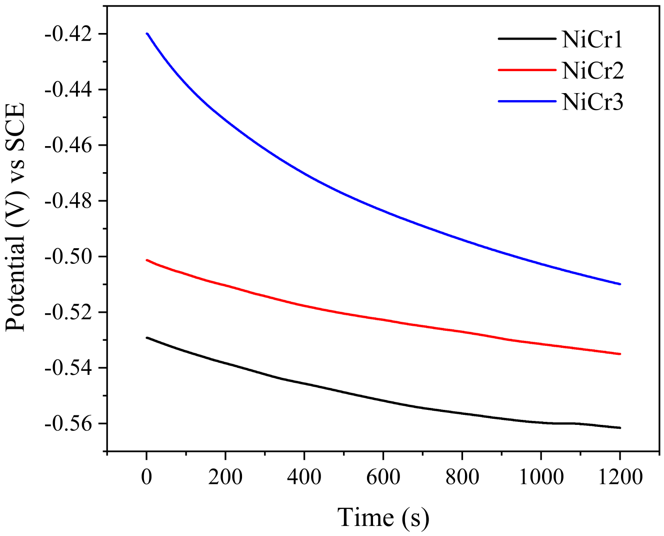

Figure 4. OCP Measurement Result

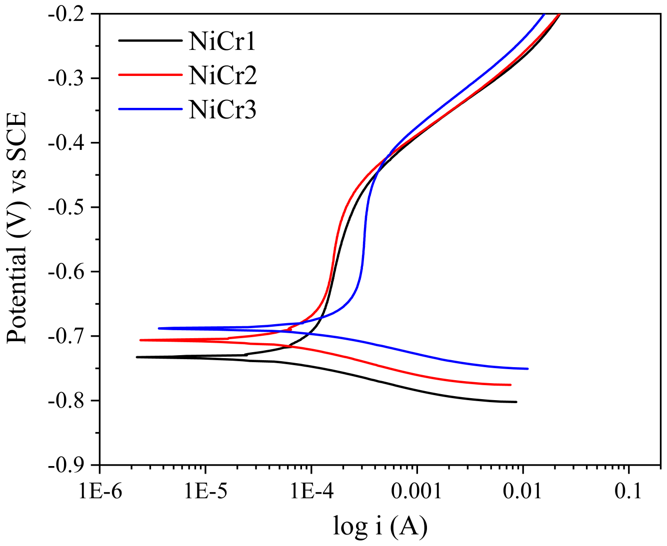

Figure 5. Potentiodynamic Polarization Curve of Various Samples

(Cano et al., 2018; Umale et al., 2019; Yi et al., 2023).

3.3 OCP

OCP was performed until 1200s, as seen in Figure 4. Various samples show similar behavior; increasing the immersion time would shift the OCP value negatively. This behavior means the dissolution of the oxide on the surface of a sample. According to an XRD analysis, Fe_3O_4 oxide was found in all samples, while FeO_2 oxide was only found in NiCr3. Generally, all oxides of iron (Fe) have low stability and, therefore, poor protection, which could dissolve into the solution during OCP measurement (Wang et al., 2020).

According to Figure 4, NiCr1, NiCr2, and NiCr3 samples have OCP values of -0.5616, -0.535, and -0.5099 V when compared to SCE. Moreover, until the 1200s measurement, all samples moved in a negative direction to reach a steady state.

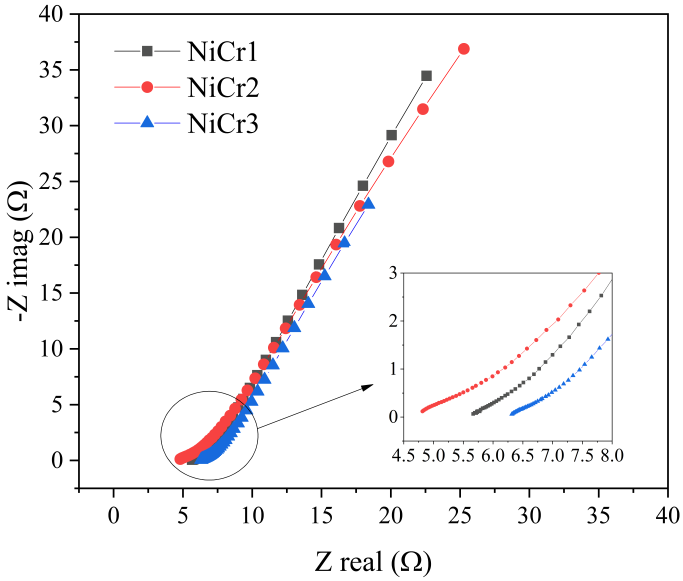

Figure 6. Nyquist Plot Curve of Various Samples

This indicates that iron oxide is still dissolving in the solution and the cathodic process is still occurring (Dagdag et al., 2020).

3.4 Potentiodinamic Polarization

Potentiodynamic polarization was conducted after the OCP measurement in 3.5% NaCl. The results of the potentiodynamic polarization scans can be seen in Figure 5. All samples show the passive area, which only extends to a small range of potential. The current suddenly increases steeply without any sign of oxygen evolution. This behavior indicates the breakdown of passive films and the initiation of pitting corrosion propagation.

Consequently, the influence of the Cl^- species on the corrosion rate of the specimens can be interpreted as a balance between the two processes competing on the specimen, stabilization of the passive film due to OH^- adsorption, and disruption of the film by Cl^- ions adsorption. Corrosion will occur when Cl^- ions overcome OH^- ions (Nady et al., 2017). The reversible formation of $Fe(OH)_{ads}$ adsorbed on the specimen is the first process during corrosion and is followed by several sequences as seen in the reaction (2-5) (Nady et al., 2017).

$$Fe + OH^- \longrightarrow FeOH^-_{ads} \tag{2}$$
$$FeOH^-_{ads} \longrightarrow FeOH_{ads} + e^- \tag{3}$$
$$FeOH_{ads} + OH^- \longrightarrow Fe(OH)_2 + e^- \tag{4}$$
$$Fe(OH)_2 + OH^- \longrightarrow FeOOH + H_2O + e^- \tag{5}$$

The presence of the Cl^- ions decreases the $Fe(OH)_{ads}$ coverage, increasing the specimens' anodic dissolution. The phenomena will be explained in the reaction (6-7) (Nady et al., 2017).

$$Fe + Cl^- \longrightarrow FeCl_{ads} + e^- \tag{6}$$
$$FeCl_{ads} \longrightarrow FeCl^+_{ads} + e^- \tag{7}$$

E_{corr} and I_{corr} were found by using the Tafel extrapolation method (see Table 2). Based on Table 2, it can be seen that increasing NiCr content in the alloy is leading to a shift in the more positive direction of E_{corr} and increasing the I_{corr} value. Furthermore, using Equation (1), the corrosion rate will be found and summarized in Table 2.

Table 2. Potentiodynamic Polarization Result

Samples	E_{corr} V (vs SCE)	I_{corr} (A/cm^2)	Corr Rate (mm/y)
NiCr1	-0.733	3.903×10^{-5}	0.1118
NiCr2	-0.706	4.228×10^{-5}	0.1212
NiCr3	-0.688	8.821×10^{-5}	0.2528

The NiCr3 sample shows more positivity than other samples, which suggests that it has nobler behavior. I_{corr} is inversely proportional to corrosion resistance. Increasing NiCr content leads to an increase in corrosion rates. NiCr1 has a corrosion rate that is less than that of other samples. The I_{corr} of this sample is about 2 times lower than NiCr3. Compared with the previous research, it has found that E_{corr} -0.711 V vs Ag/AgCl, I_{corr} 1.52×10^{-4}, and corrosion rate 0.3265 mm/y (Sopiyan et al., 2024). Therefore, presenting NiCr in the alloy of around 0.434 g could decrease the corrosion rate, but increasing the NiCr content in the alloy promoted an increase in corrosion rate.

Nady et al. (2017) investigated carbon steel (0.34 C, 0.93 Mn, 0.26 Si, 0.02 S, 0.04 P, 0.01 Cr, 0.02 Ni, and Fe balance) in 3.5% NaCl found E_{corr} -0.9996 V vs SCE and I_{corr} 5.49×10^{-5} A/cm^2. This results in less negative E_{corr} than present research due to less Ni and Cr content in the carbon steel. Wang et al. (2016) found E_{corr} Ni -77 V vs Ni/NiF$_2$ and E_{corr} Cr -507 V vs Ni/NiF$_2$. Moreover, Wang et al. (2016) have found that increasing the Cr content tends to increase a mass loss which is in perfect agreement with the potentiodynamic polarization result. Furthermore, Chen et al. (2021) found that increasing the corrosion rate of dual-phase steel attributed due to present martensite could enhance the micro-galvanic effect. Based on the microstructure and XRD evaluations, an increase in NiCr content led to an increase in the martensitic phase. Hence, increasing the NiCr content in the alloy promoting to decrease corrosion resistance.

3.5 EIS

Figure 6 represents the Nyquist plot for various samples. There is just one loop seen in each sample, which indicates that each sample has one time constant. Moreover, the highest loop tends to have higher corrosion resistance as seen in the NiCr1 sample (Nikitasari et al., 2022).

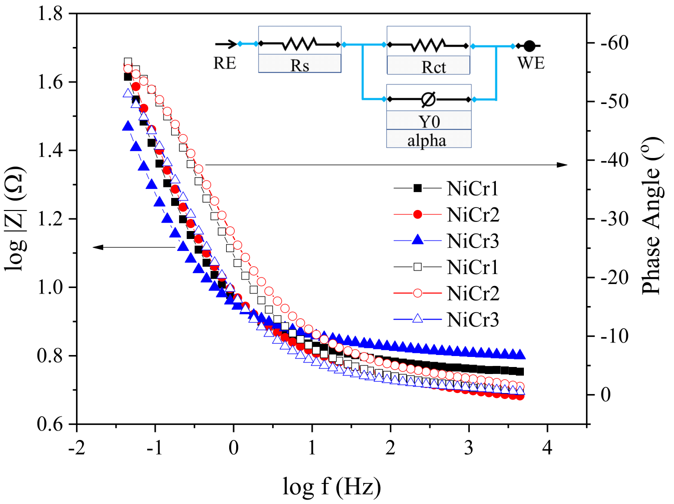

Figure 7. Bode Plot Curve of Various Samples

Figure 7 represents the Bode plot of various samples. One phase maxima was present at a lower frequency, which is attributed to the appearance of the protective oxide film. The lowest phase maxima are found in the NiCr3 sample, which indicates a higher corrosion rate (Wang et al., 2023b). The total impedance magnitude value of the samples increases with a decrease in the NiCr content, implying a decrease in the corrosion rate due to the passive film growth till the steady state is achieved (Nady et al., 2017).

Table 3. Charge Transfer Resistance and Solution Resistance

Samples	Rct (Ω)	Rs (Ω)
NiCr1	11.6×10^{7}	5.730
NiCr2	9.75×10^{7}	4.846
NiCr3	4.24×10^{7}	6.373

Rct is the charge transfer resistance, and Rs is the 3.5% NaCl solution resistance. Rct and Rs were found by fitting data from an electrical equivalent circuit (EEC) in Figure 7 and those values are presented in Table 3. Increasing the Rct value signifies improving the corrosion resistance (Nikitasari et al., 2022). NiCr1 has the maximum Rct value and highest corrosion resistance among the other samples, consistent with the potentiodynamic polarization result. Nikitasari et al. (2022) have found that a reduction in the corrosion rate is in line with an increase in the Rct values due to charge transfer from solution to steel and vice versa inhibited due to an increase in inhibitor concentration.

3.6 Hardness

Figure 8 shows the average hardness of various samples. Less hardness is found in sample NiCr1, and higher hardness is found in the NiCr3 sample. The perfect agglomeration of the NiCr addition also indicates an increase in hardness. Compared to the previous research, it can be seen that adding NiCr could enhance the average hardness of samples from 510 to 581 HV (Sopiyan et al., 2024). Martensitic formation in the welding layer leads to an increase in hardness (Faria et al., 2019). Katiyar et al. (2019) found that martensitic steel was held at 950°C for 12 minutes and followed by quenching in oil media, resulting in a hardness of 65.84±0.52 HRC (≈970HV). Based on the microstructure and XRD observations, it can be seen that an increase in NiCr content led to an increase in the martensitic phase (See Figure 3 and Table 1). Hence, increasing the NiCr content in the alloy led to increased hardness.

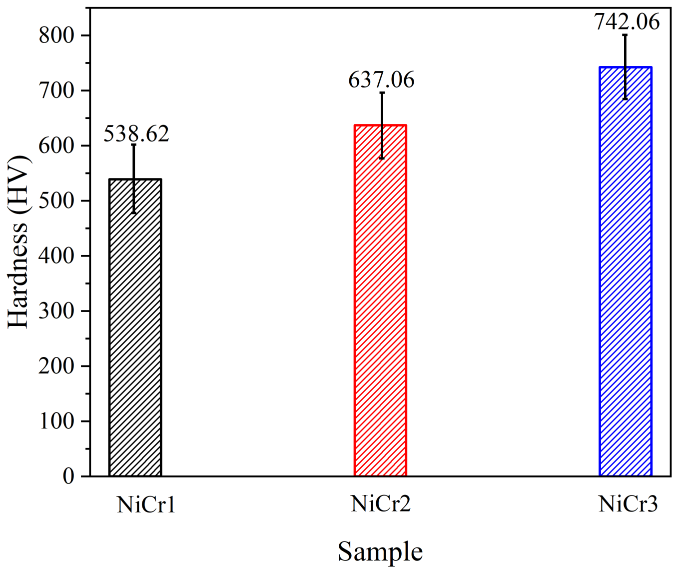

Figure 8. Average Hardness of Various Samples

4. CONCLUSIONS

Various NiCr contents were successfully added to the alloy. Presenting NiCr in the alloy of around 0.434 g leads to an increase in hardness and corrosion resistance. Increasing NiCr content in the alloy resulted in an increase in hardness and a decrease in corrosion resistance. The presence of a certain amount of Ni contributes to the formation of lower transformation phases, including martensite. The incorporation of Cr plays an important role in promoting the formation of acicular ferrite. Hardness increases due to martensitic formation in the welding layer, but this could result in a micro-galvanic effect, which decreases corrosion resistance. This research outcome could be utilized on excavator blades to enhance their hardness and corrosion resistance, which would lead to an increase in their remaining lifespan.

5. ACKNOWLEDGMENT

Authors are grateful for the support of experimental works by project BLU POK funding Fakultas Teknik Universitas Negeri Jakarta (Rector assignment agreement No. 866/UN39/HK.02/ 2023 and with Dean assignment agreement No. T/023/5.FT/ Kontrak-Penelitian/PT.01.03/III/2023).

REFERENCES

Astafurova, E., K. Reunova, E. Melnikov, M. Panchenko, S. Astafurov, A. Luchin, and E. Kolubaev (2023). A Comparison of Low-Temperature Deformation Behavior and Fracture in Low-Carbon Steel Specimens Obtained by Electron Beam Additive Manufacturing and Conventional Casting and Normalization. *Materials*, **16**(1); 446

Cano, H., I. Díaz, D. de la Fuente, B. Chico, and M. Morcillo (2018). Effect of Cu, Cr and Ni Alloying Elements on Mechanical Properties and Atmospheric Corrosion Resistance of Weathering Steels in Marine Atmospheres of Different Aggressivities. *Materials and Corrosion*, **69**(1); 8–19

Chen, H., Z. Lv, L. Lu, Y. Huang, and X. Li (2021). Correlation of Micro-Galvanic Corrosion Behavior with Corrosion Rate in the Initial Corrosion Process of Dual Phase Steel. *Journal of Materials Research and Technology*, **15**; 3310–3320

Dagdag, O., Z. Safi, N. Wazzan, H. Erramli, L. Guo, A. M. Mkadmh, and A. El Harfi (2020). Highly Functionalized Epoxy Macromolecule as an Anti-Corrosive Material for Carbon Steel: Computational (DFT, MDS), Surface (SEM-EDS) and Electrochemical (OCP, PDP, EIS) Studies. *Journal of Molecular Liquids*, **302**; 112535

Das, B., K. Sawrav, S. B. Singh, and P. P. Bandyopadhyay (2021). Tribological Behaviour of the Hardfacing Alloys Utilised to Fabricate the Wear Parts of an Excavator Bucket. *Transactions of the Institute of Metal Finishing*, **99**(3); 153–161

de Almeida, M. R. H., E. P. Barbano, M. G. Zacarin, M. M. de Brito, P. C. Túlio, and I. A. Carlos (2016). Electrodeposition of CuZn Films from Free-of-Cyanide Alkaline Baths Containing EDTA as Complexing Agent. *Surface and Coatings Technology*, **287**; 103–112

Durmuşoğlu, Ş., M. Türker, and M. Tosun (2015). Effect of Welding Parameters on the Mechanical Properties of GMA-Welded HY-80 Steels. *Materialpruefung/Materials Testing*, **57**(10); 866–871

Faria, D., P. Brito, P. A. Ramos, L. P. Resende, and D. António (2019). Experimental Investigation of Cooling Behavior and Residual Stresses for Quenching with Vegetable Oils at Different Bath Temperatures. *Journal of Cleaner Production*, **216**; 230–238

Galchenko, N., S. Raskoshniy, B. Dampilon, and K. Kolesnikova (2019). Features of Crystallization of Welded Seams from Diverse Materials at Electron Beam Welding on the Example of Highly Steel and Copper. In *AIP Conference Proceedings*, volume 2167. pages 020110–1–020110–4

Huang, S., D. Sun, and W. Wang (2015). Microstructures and Properties of Ni Based Composite Coatings Prepared by Plasma Spray Welding with Mixed Powders. *International Journal of Refractory Metals and Hard Materials*, **52**; 36–43

Jorge, L. D. J., V. S. Cândido, A. C. R. D. Silva, F. D. C. Garcia Filho, A. C. Pereira, F. S. D. Luz, and S. N. Monteiro (2018). Mechanical Properties and Microstructure of SMAW Welded and Thermically Treated HSLA-80 Steel. *Journal of Materials Research and Technology*, **7**(4); 598–605

Justus Panicker, C. T. and V. Senthilkumar (2023). Rotational Arc Based Dual Wire Arc Additive Manufacturing of Low Alloy Steel with Nichrome Inclusions for Improved Mechanical Properties. *Materials Letters*, **332**; 133498

Katiyar, P. K., S. Misra, and K. Mondal (2019). Comparative Corrosion Behavior of Five Microstructures (Pearlite, Bainite, Martensite, Austenite, and Ferrite) of a 0.4% Carbon Steel in Dilute Sulfuric Acid. *Metallurgical and Materials Transactions A: Physical Metallurgy and Materials Science*, **50**(3); 1218–1232

Kong, H., C. Xu, C. Bu, C. Da, J. Luan, Z. Jiao, G. Chen, and C. Liu (2019). Hardening Mechanisms and Impact Toughening of a High-Strength Steel Containing Low Ni and Cu Additions. *Acta Materialia*, **172**; 150–160

Kumar, S., M. Kumar, and A. Handa (2020). Erosion Corrosion Behaviour and Mechanical Properties of Wire Arc Sprayed Ni-Cr and Ni-Al Coating on Boiler Steels in a Real Boiler Environment. *Materials at High Temperatures*, **37**(6); 370–384

Kuptsov, K., M. Antonyuk, A. Bondarev, A. Sheveyko, and D. Shtansky (2021). Electrospark Deposition of Wear and Corrosion Resistant Ta (Zr) C-(Fe, Mo, Ni) Coatings to Protect Stainless Steel from Tribocorrosion in Seawater. *Wear*, **486**(August); 204094

Lee, H.-j. and H.-w. Lee (2015). Effect of Cr Content on Microstructure and Mechanical Properties of Low Carbon Steel Welds. *International Journal of Electrochemical Science*, **10**(10); 8028–8040

Li, Y. J., T.-S. Dong, B. G. Fu, G. L. Li, and Q. Liu (2021). Study of the Microstructure and Properties of Cold Sprayed Nicr Coating. *Journal of Materials Engineering and Performance*, **30**(12); 9067–9077

Li, Z., Y. Zhang, K. Dong, and Z. Zhang (2022). Research Progress of Fe-Based Superelastic Alloys. *Crystals*, **12**(5); 602

Liu, P., J. Y. Hu, H. X. Li, S. Y. Sun, and Y. B. Zhang (2020). Effect of Heat Treatment on Microstructure, Hardness and Corrosion Resistance of 7075 Al Alloys Fabricated by Slm. *Journal of Manufacturing Processes*, **60**; 578–585

Ma, Y., D. Cuiuri, C. Shen, H. Li, and Z. Pan (2015). Effect of Interpass Temperature on *In-situ* Alloying and Additive Manufacturing of Titanium Aluminides Using Gas Tungsten Arc Welding. *Additive Manufacturing*, **8**; 71–77

Nady, H., M. M. El-Rabiei, and M. Samy (2017). Corrosion Behavior and Electrochemical Properties of Carbon Steel, Commercial Pure Titanium, Copper and Copper–Aluminum–Nickel Alloy in 3.5% Sodium Chloride Containing Sulfide Ions. *Egyptian Journal of Petroleum*, **26**(1); 79–94

Nikitasari, A., G. Priyotomo, A. Royani, and S. Sundjono (2022). Exploration of *Eucheuma* Seaweed Algae Extract as a Novel Green Corrosion Inhibitor for API 5L Carbon Steel in Hydrochlorid Acid Medium. *International Journal of Engineering*, **35**(6); 1209–1216

Nikko Steel (2014). Manufacturers Of A Diverse Range Of Advanced Welding Consumables. https://www.nikkosteel.co.id/

Okechukwu, C., O. A. Dahunsi, P. K. Oke, I. O. Oladele, and M. Dauda (2018). Review on Hardfacing As Method of Improving the Service Life of Critical Components Subjected to Wear in Service. *Nigerian Journal of Technology*, **36**(4); 1095

Pauzi, G. A., A. S. Samosir, S. R. Sulistiyanti, and W. Simanjuntak (2023). Electrochemical Performance of Galvanic Cell with Silver Coated Cathode in One Compartment System Using Seawater as Electrolyte. *Science and Technology Indonesia*, **8**(1); 25–31

Saeedi, R., R. Shoja Razavi, S. R. Bakhshi, M. Erfanmanesh, and A. Ahmadi Bani (2021). Optimization and Characterization of Laser Cladding of Nicr and NiCr–TiC Composite Coatings on AISI 420 Stainless Steel. *Ceramics International*, **47**(3); 4097–4110

Singh, J., S. S. Chatha, and B. S. Sidhu (2020). Effect of Surface Alloying on Wear Behaviour of EN-47 Steel. *Materials Today: Proceedings*, **21**; 1340–1349

Soliz, A., D. Guzmán, L. Cáceres, and F. M. G. Madrid (2022). Electrochemical Kinetic Analysis of Carbon Steel Powders Produced by High-Energy Ball Milling. *Metals*, **12**(4); 665

Sopiyan, Syaripuddin, A. Ahmad, D. Nanto, S. D. Yudanto, and F. B. Susetyo (2024). Enhancement In The Hardness And Corrosion Resistance Of Mild Steel Surfaces By Nickel-Chromium Addition And Rapid Cooling After Welding. *Journal of Applied Science and Engineering*, **27**(6); 2655–2666

Syamsuir, B. Soegijono, S. D. Yudanto, B. Basori, M. K. Ajiriyanto, D. Nanto, and F. B. Susetyo (2023). Electrolyte Temperature Dependency of Electrodeposited Nickel in Sulfate Solution on the Hardness and Corrosion Behaviors. *International Journal of Engineering Transactions C: Aspects*, **36**(6); 1193–1200

Syaripuddin, Sopiyan, S. Aditya, S. D. Yudanto, and F. B. Susetyo (2023). Synthesis of Hard Layer by Titanium Addition During Welding Process and Quenched Directly. *International Journal of Engineering Transactions C: Aspects*, **36**(03); 532–539

Tanaka, T., N. Maruyama, N. Nakamura, and A. J. Wilkinson (2020). Tetragonality of Fe-C Martensite - a Pattern Matching Electron Backscatter Diffraction Analysis Compared to X-Ray Diffraction. *Acta Materialia*, **195**; 728–738

Umale, T., D. Salas, B. Tomes, R. Arroyave, and I. Karaman (2019). The Effects of Wide Range of Compositional Changes on the Martensitic Transformation Characteristics of Nitihf Shape Memory Alloys. *Scripta Materialia*, **161**; 78–83

Wang, P., L. Zhang, Z. Cheng, H. Xiong, R. Zuo, Y. Jiu, and D. Xu (2023a). Effect of Y on Interface Characteristics and Mechanical Properties of Brazed Diamond with Ni-Cr Filler Alloy. *Diamond and Related Materials*, **132**; 109645

Wang, X., Y. Tao, X. Yang, Y. Deng, D. Zhu, D. Dong, and T. Ma (2023b). Enhanced Corrosion Resistance and Hardness of CoCrCuFeNi Alloy under High-Pressure Solidification. *Intermetallics*, **154**(November); 107778

Wang, Y., Q. Zhou, K. Li, Q. Zhong, and Q. B. Bui (2015). Preparation of Ni-W-SiO_2 Nanocomposite Coating and Evaluation of Its Hardness and Corrosion Resistance. *Ceramics International*, **41**(1); 79–84

Wang, Y. L., Q. Wang, H. J. Liu, and C. L. Zeng (2016). Effect of Grain Refinement on the Corrosion of Ni-Cr Alloys in Molten (Li,Na,K)F. *Corrosion Science*, **109**; 43–49

Wang, Z., Z. Feng, and L. Zhang (2020). Effect of High Temperature on the Corrosion Behavior and Passive Film Composition of 316 L Stainless Steel in High H_2S-Containing Environments. *Corrosion Science*, **174**; 108844

Xu, Q., J. Zhang, C. Mao, X. Li, F. Guo, M. Zhang, and P. Peng (2022). Cu-Induced Enhancement of Interfacial Bonding for Brazed Diamond Grits with Ni-Cr Filler Alloys. *International Journal of Refractory Metals and Hard Materials*, **106**; 105874

Yi, Y., J. Xing, H. Jiang, S. Long, and Q. Wang (2023). Effect of Ni Content on Microstructure, Mechanical Properties, and Abrasion Behavior of Fe-B-C Alloy. *Tribology Transactions*, **66**(2); 238–248

Zhang, M., L. Li, J. Ding, Q. Wu, Y. D. Wang, J. Almer, and Y. Ren (2017). Temperature-Dependent Micromechanical Behavior of Medium-Mn Transformation-Induced-Plasticity Steel Studied by *In situ* Synchrotron X-Ray Diffraction. *Acta Materialia*, **141**; 294–303